STRESS ANALYSIS and **FATIGUE** of welded structures

A. Chattopadhyay, G. Glinka, M. El-Zein, J. Qian and R. Formas

ABSTRACT

Fatigue analyses of weldments require detailed knowledge of the stress fields in critical regions. The stress information is subsequently used for finding high local stresses where fatigue cracks may initiate and for calculating stress intensity factors and fatigue crack growth. The method proposed enables the determination of the stress concentration and the stress distribution in the weld toe region using a special shell finite element modelling technique. The procedure consists of a set of rules concerning the development of the finite element mesh necessary to capture the bending and membrane structural stresses. The structural stress data obtained from the shell finite element analysis and relevant stress concentration factors are subsequently used to determine the peak stress and the non-linear through-thickness stress distributions. The peak stress at the weld toe is subsequently used for the determination of fatigue crack initiation life. The stress distribution and the weight function method are used for the determination of stress intensity factors and for the analysis of subsequent fatigue crack growth.

IIW-Thesaurus keywords: Structural analysis; Stress distribution; Finite element analysis.

2

1 Introduction

Fatigue processes originate at stress concentration points, such as the weld toe in weldments. Both the fatigue crack initiation and propagation stages are controlled by the magnitude and the distribution of stresses in the potential crack plane. The peak stresses at the weld toe can be calculated using stress concentration factors, available in the literature, and appropriate reference stresses. These stress concentration factors are unique for given geometry and mode of loading. However, weldments are often subjected to multiple loading modes, and therefore it is not easy to define a unique nominal or reference stress. For this reason, the use of classical stress concentration factors is limited to simple geometry and load configurations for which they were derived. This problem can be resolved by using the hot spot or structural stress, σ_{hs} concept applied initially in the offshore structures industry [1]. If the stress concentration factors, based on the hot spot stress, σ_{hs} as the reference (or nominal stress), are known then the shell or coarse 3D finite element mesh models [2] can be used to determine only the hot spot stress at the weld toe and subsequently to determine the peak stress by using appropriate stress concentration factors. Unfortunately, the hot spot stress based stress concentrations factors vary for the same geometry depending on the type of loading, i.e. such stress concentration factors are not unique for a given geometry. This is a serious

drawback if various multiple loads are applied to the same weldment or welded structures.

The purpose of the method discussed below is to find such an approach that would require only stress concentration factors independent of the load configuration and appropriate reference stresses to be used. The only parameters needed for estimating the stress peak and the stress distribution induced by any combination of loads are only the geometrically unique stress concentration factors and appropriate reference or nominal stresses.

## 2 The nature of the stresses in the weld toe region

The stress state at the weld toe is multi-axial in nature. But the plate surface is usually free of stresses, and therefore the stress state at the weld toe is in general reduced to one non-zero shear and two in-plane normal stress components (Figure 1). Due to stress concentration at the weld toe the stress component, σ_{yy} normal to the weld toe line is the largest in magnitude and it is predominantly responsible for the fatigue damage accumulation in this region. Therefore, it is sufficient in practice to consider for the fatigue analysis of welded joints only the stress component σ_{yy}, i.e. its magnitude and distribution across the plate thickness.

a) The overall geometry

b) The stress state at the weld toe

Figure 1 – Stress state in the weld toe region of a welded joint
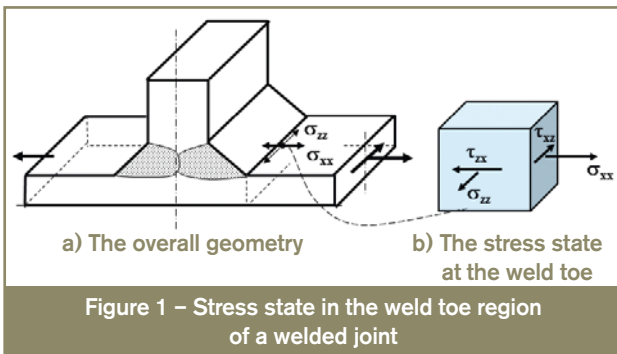
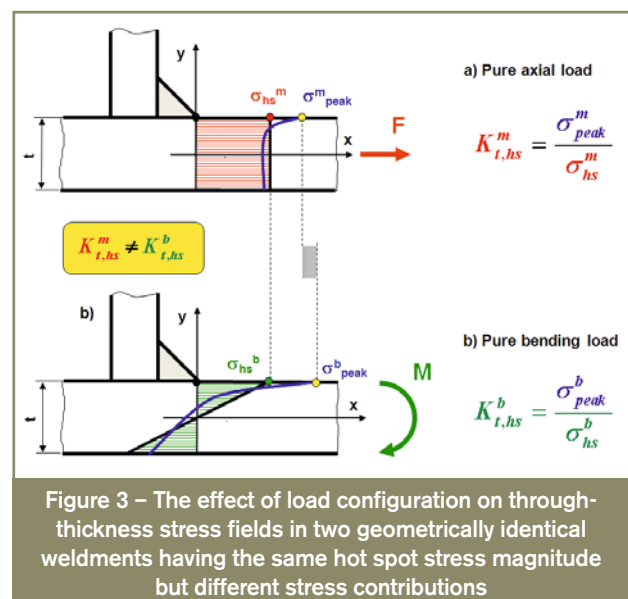# 3 The hot spot stress and the stress concentration factor

The nominal stress, σ_n in a plate without any attachments or notches [Figure 2 a)] would be equal to that one determined using the simple tension or/and bending stress formula. The existence of the attachment changes the stiffness in the weld toe region resulting in the stress concentration and non-linear through-thickness distribution as shown in Figure 2 b). However the nominal membrane and bending stresses, actually nonexistent in the welded joint, are the same as in the unwelded plate. Unfortunately, determination of meaningful nominal stress in complex welded structures is difficult and often non-unique.

Therefore the structural stress, σ_{hs} often termed as the 'hot spot stress', is used in some cases. The hot spot stress has the advantage that it accounts for the effect of the global geometry of the structure and the existence of the weld, but it does not account for the micro-geometrical effects [Figure 2 b)] such as the weld toe radius, r, and weld angle, Θ. Typical stress distributions in a welded connection with fillet welds are shown in Figure 2 b). These various stress
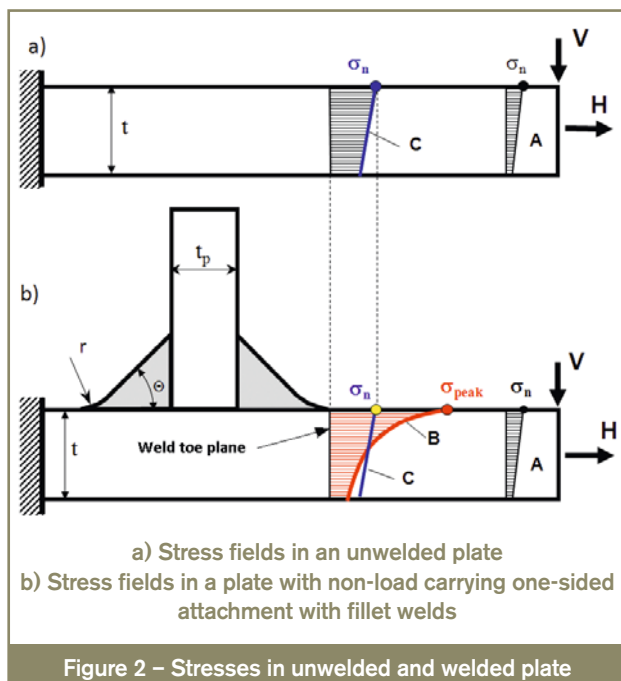
distributions are defined as follows; (A) represents the remote normal through-thickness stress distribution away from the weld, (B) the actual through-thickness normal stress distribution in the weld toe plane, (C) the statically equivalent linearized normal stress distribution in the weld toe plane, i.e. the stress distribution (C) yields the same resultant force and bending moment as the actual stress distribution (B). The linearized stress distribution (C) is independent of the micro-geometrical weld parameters such as the weld radius toe, r, and the weld angle, Θ, contrary to the stress distribution (B) which does depend on these features. The statically equivalent linearized stress distribution (C) can be characterized by two parameters, i.e. the magnitude of the hot spot stress, σ_{hs} and the slope.

The stress concentration factor and the peak stress are dependent on the magnitude and also the slope (gradient) of the linearized stress field C (Figure 3). Therefore the same hot spot stress ($\sigma_{hs}^{1,a} = \sigma_{hs}^{1,b}$), as seen in Figure 3, may 'produce' different stress concentration factors and different peak stresses, σ_{peak}. For this reason the hot spot stress alone is not sufficient for the determination of the load independent stress concentration factors. In order to define a unique stress concentration factor dependent on the geometry only both the magnitude and the gradient of the linearized (hot spot) stress must be accounted for. Therefore, Niemi [3] has proposed to decompose the linearized through-thickness stress field (Figure 2) into the uniformly distributed membrane (axial) stress field, σ_{hs}^m and the anti-symmetric bending stress field, σ_{hs}^b. This is a very useful concept because it captures the stress gradient ($\sigma_{hs}^m / \sigma_{hs}^b$) around the hot spot stress location. However, in order to determine appropriate magnitude of the peak stress, σ_{peak}, the stress concentration for pure axial load ($K_{t,hs}^m$) and pure bending load ($K_{t,hs}^b$) need to be known. The advantage of using two stress concentration factors $K_{t,hs}^m$ and $K_{t,hs}^b$ lies in the fact that they are independent of the load magnitude and are unique for a given geometry. In addition, the nominal stresses and the hot spot stresses for pure axial loading are the same, and analogously the same applies to bending load. Therefore the classical

a) Stress fields in an unwelded plate

b) Stress fields in a plate with non-load carrying one-sided attachment with fillet welds

Figure 2 – Stresses in unwelded and welded plate

a) Pure axial load

$$K_{t,hs}^m = \frac{\sigma_{peak}^m}{\sigma_{hs}^m}$$

$$K_{t,hs}^m \neq K_{t,hs}^b$$

b) Pure bending load

$$K_{t,hs}^b = \frac{\sigma_{peak}^b}{\sigma_{hs}^b}$$

Figure 3 – The effect of load configuration on through-thickness stress fields in two geometrically identical weldments having the same hot spot stress magnitude but different stress contributions

3

stress concentration $K_{t,hs}^m$ and $K_{t,hs}^b$ factors based on the nominal stress can be used. The peak stress, σ_{peak}, necessary for the prediction of fatigue crack initiation can be finally determined as the sum of the membrane and pure bending load contribution.

$$\sigma_{peak} = \sigma_{hs}^m \cdot K_{t,hs}^m + \sigma_{hs}^b \cdot K_{t,hs}^b \tag{1}$$

Thus, in order to determine the peak stress, σ_{peak}, the axial and bending hot spot stresses σ_{hs}^m and σ_{hs}^b respectively and appropriate stress concentration factors $K_{t,hs}^m$ and $K_{t,hs}^b$ must be known. Therefore, it may be informative at this moment to clarify the difference between the linearized stress field and the classical nominal stress and various stress concentration factor definitions used in practice. The difference between the classical nominal stress and the original hot spot stress definition lies in the fact that the hot spot stresses σ_{hs}^m and σ_{hs}^b are uniquely defined at any point along the weld toe (Figure 4). They can be determined by linearization of the through-thickness stress below the point on the weld toe line where the peak stress needs to be determined.

The relationships between the actual through-thickness stress distribution and hot spot stresses σ_{hs}^m and σ_{hs}^b are given by Equations (2) and (3) respectively and they represent the average membrane and bending stress contributions.

$$\sigma_{hs}^m = \frac{\int_t^0 \sigma(x, y = 0)dx}{t} \tag{2}$$

$$\sigma_{hs}^b = \frac{6 \cdot \int_t^0 \sigma(x, y = 0)xdx}{t^2} \tag{3}$$

Definitions and the method of determination of stresses σ_{hs}^m and σ_{hs}^b at points A and B (Figure 4) on the weld toe line are the same and the stress concentration factors $K_{t,hs}^m$ and $K_{t,hs}^b$ at those points are also the same if the weld geometry and dimensions are the same. Therefore, in order to determine the peak stress σ_{peak}, at point A or B the same stress concentration factors $K_{t,hs}^m$ and $K_{t,hs}^b$ can be used when correctly associated with the hot spot membrane σ_{hs}^m and bending σ_{hs}^b stresses at those points. It is
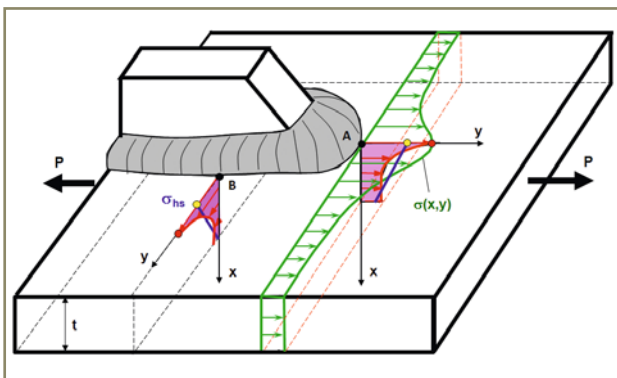
worth noting that the definition of the classical nominal stress around point B (Figure 4) is very vague in this case.

In the case of shell finite element analysis the linearized through-thickness stress is the final result of the analysis and can be easily extracted from the final output data.

4. Stress concentration factors for fillet welds

The hot spot stresses under pure axial and pure bending loads are the same as the nominal stresses ($\sigma_{hs}^m = \sigma_n^m$ and $\sigma_{hs}^b = \sigma_n^b$) and therefore the classical stress concentration factors can be used in Equation (1). Extensive literature search was carried out [4-7] for this reason and several stress concentration factor solutions were compared with each other and verified using in-house finite element data. The most universal were the stress concentration factors supplied by Japanese researchers [7] and they are discussed below. The generic geometrical configurations used for producing these stress concentration factors were the T-butt and cruciform welded joints shown in (Figure 5) and (Figure 6) respectively.
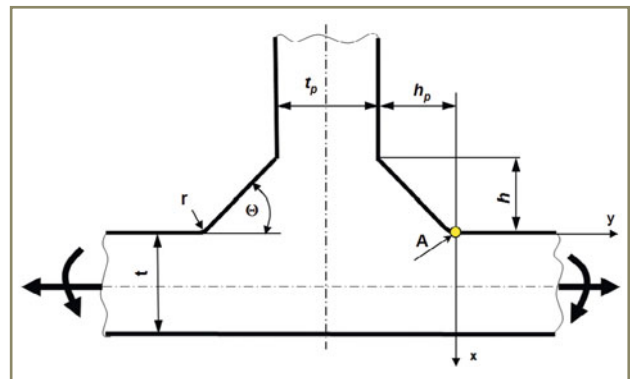

Figure 5 – Geometry and dimensions of a T-butt welded joint subjected to axial and bending load
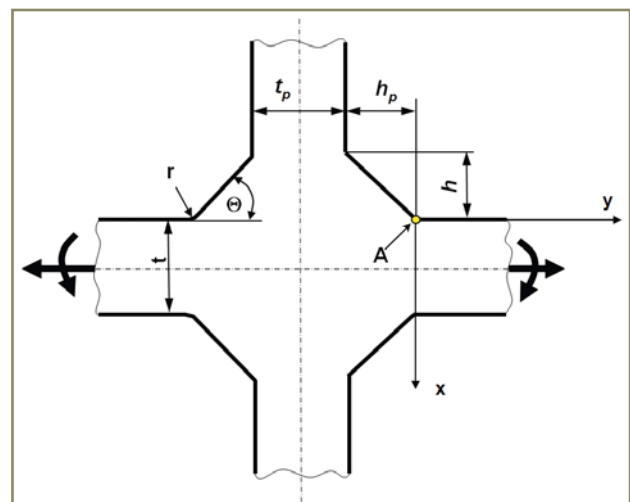

Figure 4 – The actual through-thickness stress distributions along the weld toe line and the linearized statically equivalent stress fields

Figure 6 – Geometry and dimensions of a cruciform welded joint subjected to axial and bending load

– Stress concentration factor near one-sided fillet weld under axial load (Figure 5, point A)

$$K_{t,hs}^m = 1 + \frac{1 - \exp\left(-0.9\Theta\sqrt{\frac{W}{2h}}\right)}{1 - \exp\left(-0.45\pi\sqrt{\frac{W}{2h}}\right)} \times \left[\frac{1}{2.8\left(\frac{W}{t}\right) - 2} \times \frac{h}{r}\right]^{0.65} \qquad (4)$$

– Stress concentration factor near one-sided fillet weld under bending load (Figure 5, point A).

$$K_{t,hs}^b = 1 + \frac{1 - \exp\left(-0.9\Theta\sqrt{\frac{W}{2h}}\right)}{1 - \exp\left(-0.45\pi\sqrt{\frac{W}{2h}}\right)} \times 1.9\sqrt{\tanh\left(\frac{2t_p}{t+2h} + \frac{2r}{t}\right)} \times$$

$$\tanh\left[\frac{\left(\frac{2h}{t}\right)^{0.25}}{1 - \frac{r}{t}}\right] \times \left[\frac{0.13 + 0.65\left(1 - \frac{r}{t}\right)^4}{\left(\frac{r}{t}\right)^{\frac{1}{3}}}\right] \qquad (5)$$

where

$$W = (t + 2h) + 0.3\,(t_p + 2h_p)$$

Equations (4) and (5) are semi-empirical in nature and have been derived using analytical solutions for stress concentrations at corners supplemented by extensive finite element stress concentration database. Their application was verified for a range of geometrical configurations limited to $0.02 \leq r/t \leq 0.16$ and $30° \leq \Theta \leq 60°$.

Similar expressions have also been derived for stress concentration factors in cruciform welded joints [7] and they apply in general to weldments with two symmetric fillet welds placed on both sides of the load carrying plate.

– Stress concentration factor for a cruciform joint subjected to an axial load (Figure 6, point A).

$$K_{t,hs}^m = 1 + \frac{1 - \exp\left(-0.9\Theta\sqrt{\frac{W}{2h}}\right)}{1 - \exp\left(-0.45\pi\sqrt{\frac{W}{2h}}\right)} \times 2.2\left[\frac{1}{2.8\left(\frac{W}{t}\right) - 2} \times \frac{h}{r}\right]^{0.65} \qquad (6)$$

– Stress concentration factor for a cruciform joint subjected to bending load (Figure 6, point A).

$$K_{t,n}^{ben} = 1 + \frac{1 - \exp\left(-0.9\Theta\sqrt{\frac{W}{2h}}\right)}{1 - \exp\left(-0.45\pi\sqrt{\frac{W}{2h}}\right)} \times \sqrt{\tanh\left(\frac{2t_p}{t+2h} + \frac{2r}{t}\right)} \times$$

$$\tanh\left[\frac{\left(\frac{2h}{t}\right)^{0.25}}{1 - \frac{r}{t}}\right] \times \left[\frac{0.13 + 0.65\left(1 - \frac{r}{t}\right)^4}{\left(\frac{r}{t}\right)^{\frac{1}{3}}}\right] \qquad (7)$$

where

$$W = (t + 4h) + 0.3(t_p + 2h_p)$$

Equations (6) and (7) are also empirical in nature and have been derived using extensive finite element stress data. The range of application for these expressions is: $r/t = 0.1\text{-}0.2$, $h/t = 0.5\text{-}1.2$, $\Theta = 30°\text{-}80°$.

5 The shell finite element model

The linear through-thickness stress field is naturally embedded in as the property of most basic shell finite elements. The output stresses are the stress components σ_{hs}^1 and σ_{hs}^2 (Figure 7) acting on each side of the plate thickness. Therefore the determination of the membrane and bending hot spot stresses requires only simple post-processing as shown below.

$$\sigma_{hs}^m = \frac{\sigma_{hs}^1 + \sigma_{hs}^2}{2} \qquad (8)$$

$$\sigma_{hs}^b = \frac{\sigma_{hs}^1 - \sigma_{hs}^2}{2} \qquad (9)$$

Unfortunately, such a simple finite element model as that one shown in Figure 7 b) is not capable of supplying sufficiently accurate stresses in the weld toe region. This is due to the fact that the critical cross-section in the actual welded joint is located at the weld toe (sections A and B, Figure 7) being away from the mid-planes intersection. In addition, the magnitude of stresses σ_{hs}^1 and σ_{hs}^2 and the resultant slope of the linear stress field depend on the distance from point 'O' [Figure 7 b)] and the size of the shell element. The shell stresses in the weld toe region depend strongly on the local stiffness of the joint and, therefore, they are sensitive to how the weld stiffness is accounted for in the finite element shell model. It is important to model the weldment and any welded structure in such a way that the hot spot shell membrane σ_{hs}^m and bending stress σ_{hs}^b in critical cross-sections [Figure 7 b)] are the same as those which would be determined from the linearization of the actual 3D stress fields, obtained analytically or from fine mesh 3D finite element model [Figure 7 a)] of the joint. In other words the shell model of the weld needs to be also included.

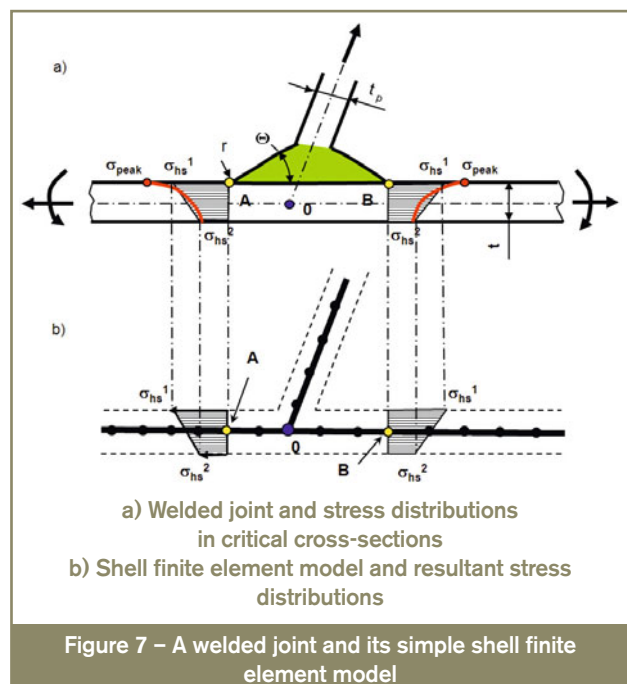Fayard, Bignonnet and Dang Van [8] have proposed a shell finite element model with rigid bars simulating the

a) Welded joint and stress distributions in critical cross-sections
b) Shell finite element model and resultant stress distributions

Figure 7 – A welded joint and its simple shell finite element model

5

weld. They have also formulated a set of rules concerning the finite element meshing in order to capture correctly the properties of the linear stress field. However, using shell elements and rigid bars was found not very convenient in practice. Therefore, a new model involving only shell elements of the same type in the entire structure was proposed.

There are two important issues concerning the shell FE modelling of welded joints namely: the simulation of the local weld stiffness and the location of the stress reference point where the stress corresponding to the actual weld toe position is to be determined. Therefore, the shell finite element model has to be constructed in such a way that the location of the stress reference point coincides with the actual position of the weld toe (Figure 7).
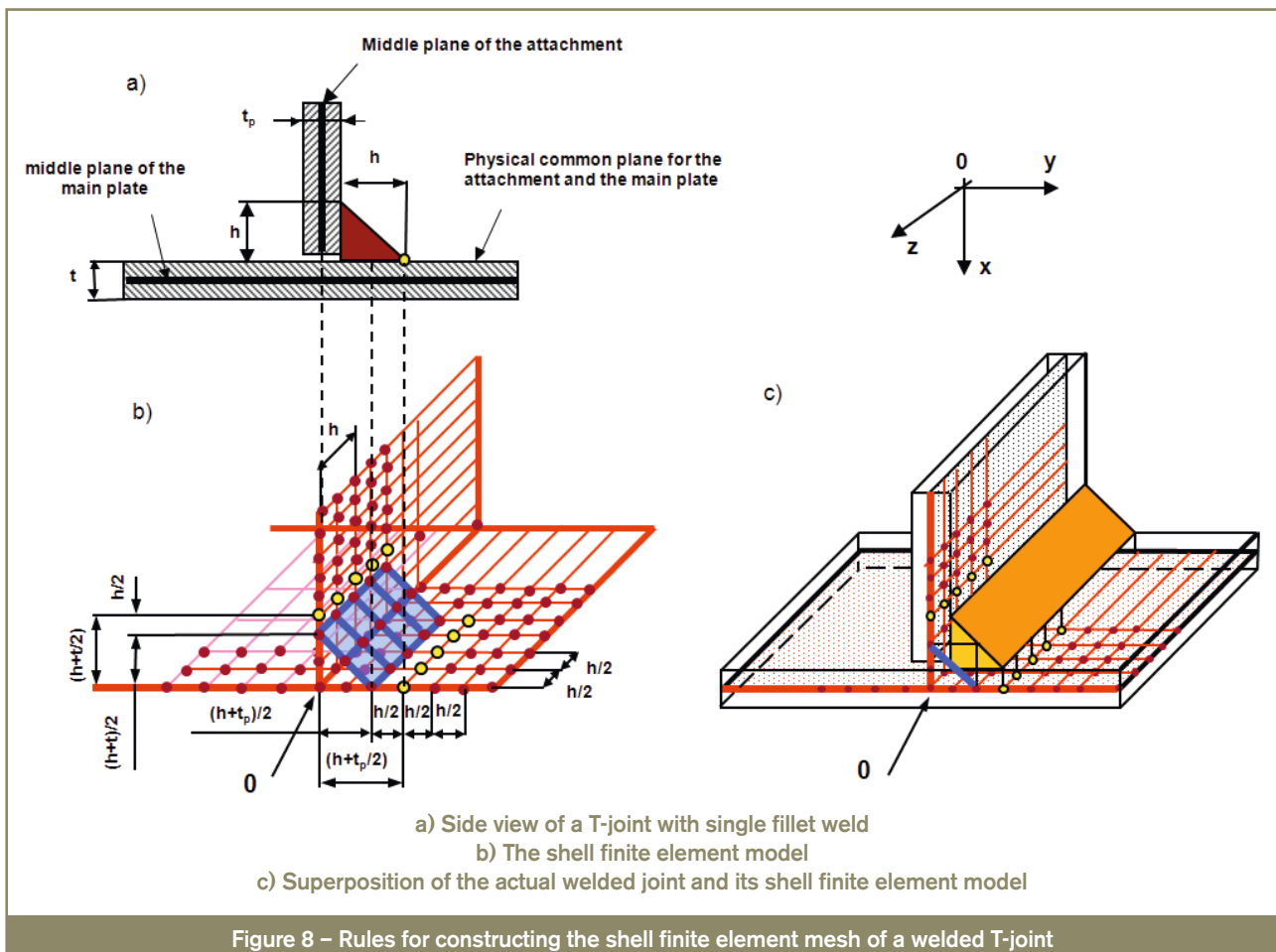
In order to assure that the global effects of the joint geometry and the weld are adequately modelled, a set of rules have been formulated concerning the construction of appropriate finite element shell model as shown in Figure 8. The meshing principles of the model are illustrated using as an example a T-welded joint. The following steps need to be carried out while creating appropriate shell finite element mesh.

a. Connect the mid-thickness plate planes [Figure 8 a) and 8 b)], and add one layer (blue) of inclined shell elements representing the weld.

b. The first and the second rows of elements adjacent to the theoretical intersection line of mid-thickness planes must be of the size $(t_p + h)/4$ in the 'x' direction for elements in the main plate and $(t + h)/4$ in the 'y' direction for elements in the attachment. The shell elements simulating the weld are subsequently attached to each plate in the middle of the weld leg length and they are spanning the first two rows of elements in each plate. The thickness of the shell elements simulating the weld is recommended to be equal to the thickness of the thinner plate being connected by the weld (i.e. either t or t_p whichever is less). All shell elements simulating the weld are of the same thickness.

All shell elements in the weld region have the same dimension in the z direction and it is equal or less than the half weld leg length, i.e. '$h/2$' or less.

c. The shell elements in the third row simulating the main plate should have the size equal to half of the weld leg length '$h/2$' in the 'x' and 'z' directions and the same '$h/2$' dimension in the 'y' and 'z' directions for elements in the attachment plate [Figure 8 b)]. The choice of such element dimensions enables to locate the reference points A at the nodal points of elements from the third row. The location of

a) Side view of a T-joint with single fillet weld
b) The shell finite element model
c) Superposition of the actual welded joint and its shell finite element model

Figure 8 – Rules for constructing the shell finite element mesh of a welded T-joint

the reference point A must coincide with the physical position of the weld toe. Thus stresses at the reference point A are the same as the nodal stresses and they can be extracted without any interpolation or additional post-processing.

d. The dimension 'z' of the first two rows of elements adjacent to the intersection of plate mid-thickness planes is dictated by the smallest element in the region, i.e. it should not be greater than half of the weld leg length '$h/2$'. It means that the first and the second rows of elements in the main plate [Figure 8 b)] have the dimension of $[(h/4 + t_p/4) \times h/2]$. The first two rows of elements in the attachment counted from the mid-plane intersection should have the size of $[(h/4 + t/4) \times h/2]$. The elements in the third row are $(h/2 \times h/2)$ in size. The spacing in the 'z' direction might need to be smaller than half of the weld leg length '$h/2$' while modelling corners of non-circular tubes or weld ends around gusset plates.

5.1 Determination of the peak stress at the weld toe

In order to determine the peak stress σ_{peak} at the weld toe it is necessary to determine the membrane σ_{hs}^m and bending σ_{hs}^b stress from the shell finite element model using Equations (8-9). Then the stress concentration factors $K_{t,hs}^m$ and $K_{t,hs}^b$ for tension and bending need to be calculated from Equations (4-5) or (6-7) by using actual dimensions of the weld. The peak stress σ_{peak} can be finally calculated from Equation (1).

The knowledge of the linear elastic peak stress σ_{peak} enables subsequently the assessment of the fatigue crack initiation life by applying the local strain-life method widely used in the automotive industry [9-12].

5.2 Determination of the through-thickness stress distribution

Because welded structures are known as having high stress concentration at weld toes and roots the fatigue crack initiation period might be relatively short and therefore fatigue life assessment based on the fatigue crack growth analysis is often required. In order to carry out a meaningful fatigue crack growth analysis appropriate stress intensity factor solutions are needed. Because of wide variety of possible configurations of the global joint geometry, the weld geometry, the crack geometry and loading reliable ready-made stress intensity solutions are seldom available. Therefore the weight function method (discussed later) seems to be a convenient and efficient solution but the through-thickness stress distribution in the prospective crack plane must be known in such a case.

It has been found that the same information, i.e. the membrane σ_{hs}^m and bending σ_{hs}^b hot spot stresses and

associated stress concentration factors $K_{t,hs}^m$ and $K_{t,hs}^b$ are sufficient for the determination of the through-thickness distribution denoted as distribution B in Figure 2 b).

The stress distribution, needed for the stress intensity factor K calculation, can be determined by using universal stress distributions proposed by Monahan [13]. Both equations shown below were derived for the through-thickness stress distribution in a T-butt weldment (Figure 5) but they can also be applied over half of the thickness in the case of cruciform weldments (i.e. for a weldment with symmetric welds located on both side of the plate as shown in Figure 6).

For pure tension loading the through-thickness stress distribution can be sufficiently accurate approximated by Equation (10).

$$\sigma^m(x) = \frac{K_{t,hs}^m \sigma_{hs}^m}{2\sqrt{2}}\left[\left(\frac{x}{r}+\frac{1}{2}\right)^{-\frac{1}{2}}+\frac{1}{2}\left(\frac{x}{r}+\frac{1}{2}\right)^{-\frac{3}{2}}\right]\frac{1}{G_m} \quad (10)$$

where

$$G_m = 1 \text{ for } \frac{x}{r} \leq 0.3$$

$$G_m = 0.06 + \frac{0.94 \times e^{-E_m T_m}}{1 + E_m^3 T_m^{0.8} \times e^{-E_m T_m^{1.1}}} \text{ for } \frac{x}{r} > 0.3$$

$$E_m = 1.05 \times \Theta^{0.18}\left(\frac{r}{t}\right)^q$$

$$q = -0.12\Theta^{-0.62}$$

$$T_m = \frac{x}{t} - 0.3\frac{r}{t}$$

For pure bending load Equation (11) is recommended:

$$\sigma^b(x) = \frac{K_{t,hs}^b \sigma_{hs}^b}{2\sqrt{2}}\left[\left(\frac{x}{r}+\frac{1}{2}\right)^{-\frac{1}{2}}+\frac{1}{2}\left(\frac{x}{r}+\frac{1}{2}\right)^{-\frac{3}{2}}\right]\frac{1-2\left(\frac{x}{t}\right)}{G_b} \quad (11)$$

where

$$G_b = 1 \text{ for } \frac{x}{r} \leq 0.4$$

$$G_b = 0.07 + \frac{0.93 \times e^{-E_b T_b}}{1 + E_b^3 T_b^{0.6} \times e^{-E_b T_b^{1.2}}} \text{ for } \frac{x}{r} > 0.4$$

$$E_b = 0.9\left(\frac{r}{t}\right)^{-\left(0.0026 + \frac{0.0825}{\Theta}\right)}$$

$$T_b = \frac{x}{t} - 0.4\frac{r}{t}$$

Equations (10-11) can be used to predict through-thickness stress distributions near fillet welds joining plates, tubes and other structural elements providing that parameters Θ, r/t, and x are within the following limits:

$$\frac{\pi}{6} \leq \Theta \leq \frac{\pi}{3} \text{ and } \frac{1}{50} \leq \frac{r}{t} \leq \frac{1}{15} \text{ and } 0 \leq x \leq t \quad (12)$$

If both membrane and bending stresses are present the resultant through-thickness stress distribution can be obtained by superposition of Equations (10) and (11).

7

$$\sigma(x) = \sigma^m(x) + \sigma^b(x) = \left[\frac{K_t^m \sigma_{hs}^m}{2\sqrt{2}} \cdot \frac{1}{G_m} + \frac{K_t^b \sigma_{hs}^b}{2\sqrt{2}} \cdot \frac{1 - 2\left(\frac{x}{t}\right)}{G_b} \right]$$

$$\left[\left(\frac{x}{r} + \frac{1}{2}\right)^{-\frac{1}{2}} + \frac{1}{2}\left(\frac{x}{r} + \frac{1}{2}\right)^{-\frac{3}{2}} \right] \tag{13}$$

Appropriate weight functions [14-15] and the stress distribution (13) make it possible to determine stress intensity factors and to subsequently simulate the fatigue crack growth in any welded structure without the labour and time consuming extensive FE numerical analyses of cracked bodies. In addition the method is self-consistent and does not require making any arbitrary adjustments.

6 Fatigue crack initiation analysis

The maximum of the peak stress $\sigma_{peak,max}$ and the peak stress range $\Delta\sigma_{peak}$ at the weld toe can be subsequently used for the calculation of the actual stresses and elastic-plastic strains at the weld toe. The most common method is the use of the Neuber [9] or the ESED [10] method and the material cyclic stress-strain curve in the form of the Ramberg-Osgood expression.

$$\frac{\left(\sigma_{peak,max}\right)^2}{E} = \sigma_{max}^a \varepsilon_{max}^a - \text{the Neuber rule} \tag{14}$$

$$\varepsilon_{max}^a = \frac{\sigma_{max}^a}{E} + \left(\frac{\sigma_{max}^a}{K'}\right)^{\frac{1}{n'}} - \text{the material Ramberg-Osgood stress-strain curve} \tag{15}$$

In order to calculate the elastic-plastic strain range and corresponding stress range the same Neuber rule associated with the stress-strain curve expanded by factor of 2 can be used.

$$\frac{\left(\Delta\sigma_{peak}\right)^2}{E} = \Delta\sigma^a \cdot \Delta\varepsilon^a \quad - \text{the Neuber rule} \tag{16}$$

$$\Delta\varepsilon^a = \frac{\Delta\sigma^a}{E} + 2\left(\frac{\Delta\sigma^a}{2K'}\right)^{\frac{1}{n'}} - \text{the expanded material stress-strain curve} \tag{17}$$

Because it is known that the Neuber rule has the tendency of overestimating the local elastic-plastic strains and stresses at high stress concentration factors the Equivalent Strain Energy Density (ESED) method can be used in the form of analogous set of equations for obtaining the maximum elastic-plastic strain and stress at the weld toe.

$$\frac{\left(\sigma_{peak,max}\right)^2}{2E} = \frac{\left(\sigma_{max}^a\right)^2}{2E} + \frac{\sigma_{max}^a}{n' + 1}\left(\frac{\sigma_{max}^a}{K'}\right)^{\frac{1}{n'}} - \text{the ESED rule} \tag{18}$$

$$\varepsilon_{max}^a = \frac{\sigma_{max}^a}{E} + \left(\frac{\sigma_{max}^a}{K'}\right)^{\frac{1}{n'}} - \text{the material Ramberg-Osgood stress-strain curve} \tag{19}$$

The same ESED rule but combined with the expanded by factor of 2 stress-strain curve is applied for calculating the elastic-plastic strain and stress range.

$$\frac{\left(\Delta\sigma_{peak}\right)^2}{2E} = \frac{\left(\Delta\sigma^a\right)^2}{2E} + \frac{2 \cdot \Delta\sigma^a}{n' + 1}\left(\frac{\Delta\sigma^a}{2K'}\right)^{\frac{1}{n'}} - \text{the ESED rule} \tag{20}$$

$$\Delta\varepsilon^a = \frac{\Delta\sigma^a}{E} + 2\left(\frac{\Delta\sigma^a}{2K'}\right)^{\frac{1}{n'}} - \text{the expanded material stress-strain curve} \tag{21}$$

The actual maximum stress σ_{max}^a at the weld toe and the actual strain range $\Delta\varepsilon^a$ obtained from Equations (14-17) or (18-21) formulate the base for calculating the number of cycles, N_i, to initiate a fatigue crack at the weld toe.

The basic fatigue material property is the strain-life equation proposed [11] by Manson and Coffin.

$$\frac{\Delta\varepsilon}{2} = \frac{\sigma_f'}{E}\left(2N_i\right)^b + \varepsilon_f'\left(2N_i\right)^c \tag{22}$$

In order to account for the mean stress effect or the existence of residual stresses the SWT [12] fatigue damage parameter can be used in association with the Manson-Coffin curve.

$$\sigma_{max}^a \frac{\Delta\varepsilon^a}{2} = \frac{\left(\sigma_f'\right)^2}{E} \cdot \left(2N_f\right)^{2b} + \varepsilon_f'\sigma_f' \cdot \left(2N_f\right)^{b+c} \tag{23}$$

Unfortunately, the strain-life method does not specify what crack size is associated with the end of the initiation period, therefore an engineering definition needs to be adopted. Based on author's experience a semi-circular crack of the initial depth of $a_i = 0.5$-0.8 mm seems to be a reasonable good assumption.

It is worth noting that there are several fatigue software packages for which the local elastic stress σ_{peak} and material curves (13) and (19) are the standard input data for automatic fatigue crack initiation life assessment. Therefore, the method described above can be associated with any available computer fatigue software package.

7 The fatigue crack growth analysis

The fatigue crack growth period is often thought to be representing almost the entire fatigue life of weldments because it is believed that the fatigue crack initiation period in welded joints is relatively short. The authors experience is that the ratio of the fatigue crack initiation life to the length of the fatigue crack growth period varies depending on the load and weld geometrical factors and its relative contribution to the total fatigue life of a weldment increases in with the decrease of the applied cyclic load and the increase of the total life. Therefore good assessments of both the fatigue crack initiation and propagation period are necessary for reasonably accurate estimation of fatigue lives of weldments subjected to cyclic loading histories.

The first and the most popular expression characterizing material properties from the point of view of the material resistance to fatigue crack growth is the Paris [16] equation.

$$\frac{da}{dN} = C(\Delta K)^m \tag{24}$$

Unfortunately, the Paris equation in its original form (24) does not account for the effect of the stress ratio R or the mean stress. Therefore the recently proposed [17, 18] Equation (25) is gaining popularity.

$$\frac{da}{dN} = C\left(K_{max}^{1-p}\Delta K^p\right)^{\gamma} \tag{25}$$

where

C, p, m and γ are material constants, K_{max} is the maximum stress intensity factor and ΔK is the stress intensity range. In the case of pulsating constant amplitude stress history ($R = 0$) Equation (25) takes the well-known form of the Paris equation.

The fatigue crack propagation life is obtained by analytical or numerical integration of the fatigue crack growth equation.

$$N_p = \int_{a_i}^{a_f} \frac{da}{C(\Delta K)^m} \quad \text{or} \quad N_p = \int_{a_i}^{a_f} \frac{da}{C\left(K_{max}^{1-p}\Delta K^p\right)^{\gamma}} \tag{26}$$

However, in order to Integrate any fatigue crack growth rate expression available in the literature the stress intensity factors K_{max} and ΔK need to be determined.

7.1 Application of the weight function method for efficient determination of stress intensity factors

In the case of simple geometry and load configurations like the edge or semi-elliptical surface crack in a plate subjected to pure bending or tension load ready-made stress intensity factor expressions can be found [19] in Handbooks of Stress Intensity Factors. Unfortunately, there are no ready-made solutions for cracks in welded structures except for a few crack configurations in simple welded joints. Therefore the weight function technique [14, 15] was employed in order to determine stress intensity factors for cracks in real welded structures.

The weight function can be understood as the stress intensity factor (Figure 9) induced by the simplest load configuration, i.e. a pair of unit splitting forces F attached to the crack surface.

There are many expressions for various weight functions but it is possible [15] to write them in one general form (27).

$$m(x,a) = K_A^P = \frac{2F}{\sqrt{2\pi(a-x)}}\left\{1 + M_1\left(1 - \frac{x}{a}\right)^{\frac{1}{2}}\right.$$

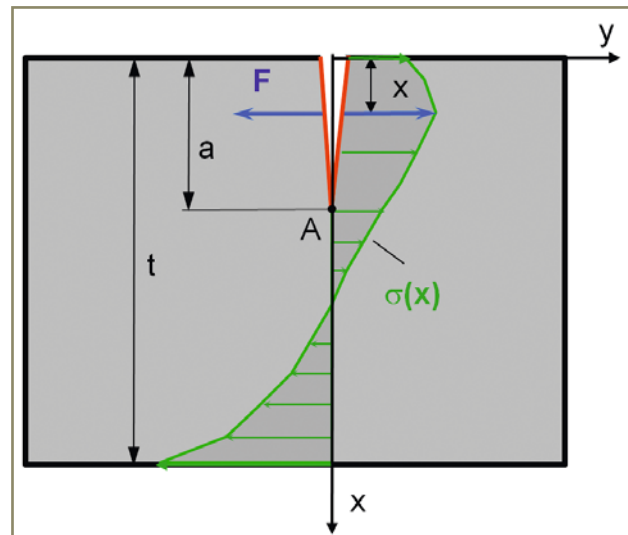$$\left. + M_2\left(1 - \frac{x}{a}\right) + M_3\left(1 - \frac{x}{a}\right)^{\frac{3}{2}}\right\} \tag{27}$$

Figure 9 – Notation for the weight function

Parameters M_1, M_2 and M_3 depend on the crack geometry and they have been derived already [15] for a variety of cracks. The M_i parameters for a single edge and surface semi-elliptical crack are given in reference [15] and listed in the Appendix.

If the weight function is known, the stress intensity factor K can be calculated by integrating the product of the stress distribution, $\sigma(x)$, in the prospective crack plane and the weight function $m(x,a)$:

$$K_A^{\sigma(x)} = \int_0^a \sigma(x) \cdot m(x,a) \cdot dx \tag{28}$$

Thus, the calculation of stress intensity factors by the weight function method for any crack, including cracks in weldments, requires the knowledge of the stress distribution, $\sigma(x)$, in the prospective crack plane in the un-cracked body [Figure 10 a)] and then the stress distribution should be virtually applied to the crack surfaces [Figure 10 b)].
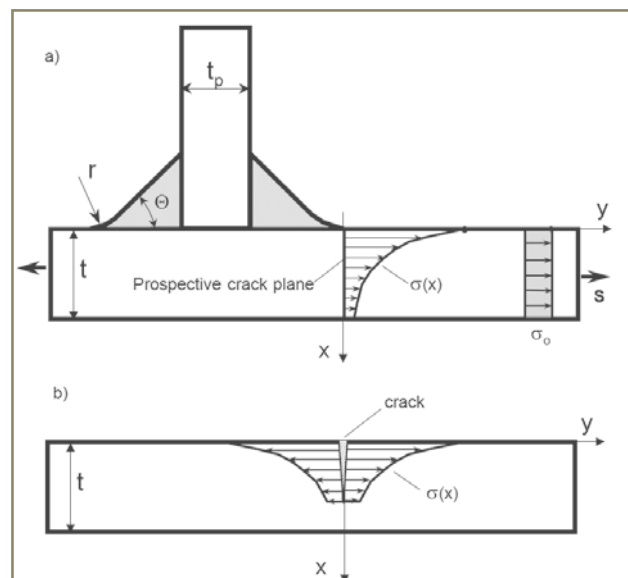

Figure 10 – The use of the weight function for an edge crack in plate for calculating the SIF for a crack in a T-butt weldment

9

Finally the product of the stress distribution $\sigma(x)$ and the weight function $m(x,a)$ needs to be integrated over the entire crack surface area [see Equation (28)]. It is to note that the stress analysis needs to be carried out only once and for an un-cracked body [Figure 10 a)].

The stress intensity factor calculations can be repeated after each crack increment induced by subsequent load cycles so the stress intensity factor is calculated for the instantaneous (actual) crack size and geometry. Such a method enables simulation of the crack growth and the evolution of the crack shape in the case of 2D planar cracks.

8 Stress and fatigue analysis of a tubular welded section subjected to constant amplitude fully reversed torsion and bending loads

Several welded structures and welded joints were studied experimentally and numerically in order to verify the validity of the proposed methodology. The welded structure shown in Figure 11, subjected to torsion and bending load, was chosen as an example for illustrating the stepwise procedure. The overall geometry of the welded joint fixed in the testing rig is also shown in Figure 11. Dimensions of selected welded tubular profiles were 4 x 4 x 23.625 in and 2 x 6 x 14.313 in and the wall thicknesses were equal to 0.312 in. The geometrical constrains of the fixture and the location of the applied load is shown in Figure 12. The welded tubular profiles were made of A22-H steel (ASTM A500 Cold Formed Steel for Structural Tubing) used often in the construction and earth moving machinery. The manual Flux Cord Arc Welding method was used to manufacture a series of specimens. The welding parameters were typical for manual welding aimed at the maximum weld penetration
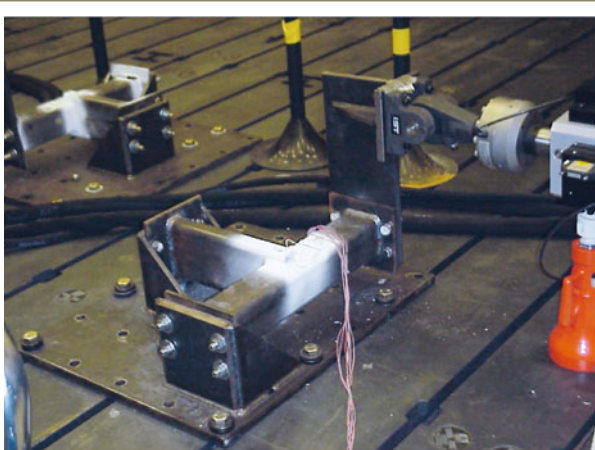

Figure 11 – The tubular welded joint subjected to torsion and bending load in the testing rig
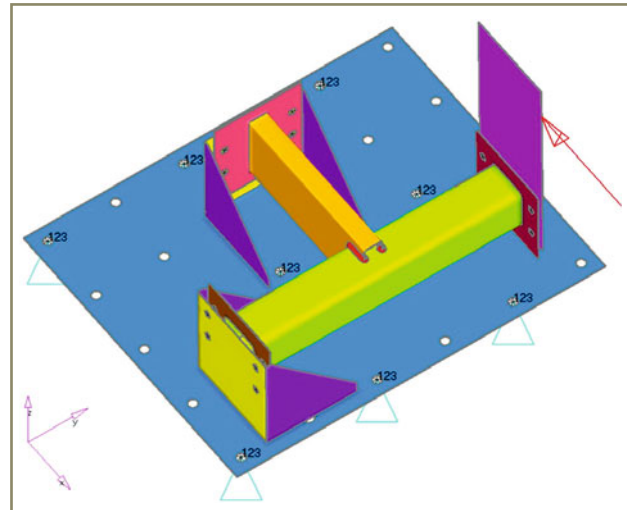

Figure 12 – Solid model of the welded joint- configuration of support points and the location of the loading force

and maximum uniformity of weld geometry along its entire length. The average weld dimensions obtained from the welding process were (see Figure 5):

$t = 0.312$ in, $t_p = 3 \times 0.312$ in, $h = 0.312$ in, $h_p = 0.312$ in, $\Theta = 45°$, $r = 0.0312$ in

The specimens were tested at two different cyclic load levels of ± 3 000 lb and ± 4 000 lb applied at the free end of the large square profile (Figure 12). The bottom base plate of the fixture was held by six screws. In order to assess anticipated scatter of experimental fatigue lives seven specimens were tested at each load level.

8.1 The shell FE stress analysis

The shell model of the analysed welded tubular joint is presented in Figure 13. The overall stress field obtained from the FE analysis of the entire structure is also shown graphically in Figure 13. Three high stress locations were identified with the highest stresses found at Location 1. Therefore detail analysis of stresses at Location 1 was undertaken. The exact location of the maximum stress was found in the region around the ending edge of the rectangular tube. The stresses of interest were those found at the reference point shown in Figure 14 of the shell model. The location of the reference point was coinciding as usual with the physical position of the weld toe in the actual weld joint. The distance between the reference point and the tube wall mid-planes intersection point in the shell FE model was equal to:

$$h + \frac{t_p}{2} = 0.312 + \frac{0.312}{2} = 0.468 \text{ in}$$

The shell stresses σ_{hs}^1 and σ_{hs}^2 on opposite sides of the tube wall (see Figure 7), obtained from the shell FE model, were used for the determination of the membrane and bending [Equations (8-9)] hot spot stresses, σ_{hs}^m and σ_{hs}^b, respectively. The peak stress at the weld toe, σ_{peak}, was determined from Equation (1). The through-
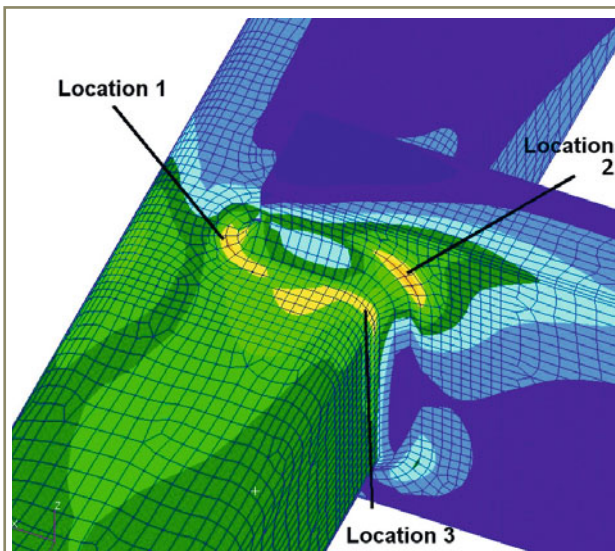
Figure 13 – The shell finite element model of the welded joint showing overall stress distribution with three distinct regions of high stresses

Figure 14 – Details of the shell FE model and the location of the reference point for determining the hot spot stress

thickness stress distribution, $\sigma(x)$, was calculated using Equations (10-11,13).

The shell stresses induced by the unit load of $P = 1.0$ lb on the two sides of the tube wall and calculated using the shell FE data were:

$\sigma_{hs}^{1} = 8.25$ psi and $\sigma_{hs}^{2} = -3.05$ psi

Therefore the hot spot stresses determined according to Equations (8) and (9) were:

$$\sigma_{hs}^{m} = \frac{\sigma_{hs}^{1} + \sigma_{hs}^{2}}{2} = \frac{8.25 + (-3.05)}{2} = 2.6 \text{ psi}$$

$$\sigma_{hs}^{b} = \frac{\sigma_{hs}^{1} - \sigma_{hs}^{2}}{2} = \frac{8.25 - (-3.05)}{2} = 5.65 \text{ psi}$$

The stress concentration factors $K_{t,hs}^{m}$ and $K_{t,hs}^{b}$ obtained from Equations (4) and (5) for geometrical dimensions $t = 0.312$ in, $t_{p} = 3t = 0.936$ in, $h = 0.312$ in, $h_{p} = 0.312$ in, $r = 0.0312$ in and $\Theta = 45°$, were $K_{t,hs}^{m} = 1.784$ and $K_{t,hs}^{b} = 2.203$. The hot spot stresses corresponding to the unit load $P = 1$ lb and the stress concentration factors inputted into Equation (1) resulted in the determination of the peak stress at the weld toe.

$\sigma_{peak} = \sigma_{hs}^{m} \cdot K_{t,hs}^{m} + \sigma_{hs}^{b} \cdot K_{t,hs}^{b} = 2.6 \times 1.784 = 5.65 \times 2.203$ $= 17.089$ psi. In order to determine stresses corresponding to the actual load $P = 3\,000$ lb or 40 000 lb the stress $\sigma_{peak} = 17.089$ psi was scaled by the factor of 3000 or 4000 depending on the applied load magnitude.

The through-thickness stress distribution $\sigma(x)$ was obtained using the universal Equations (10-11 and 13) and geometrical parameters, hot spot stresses and stress concentration factors listed above. The through-thickness stress distribution induced by the applied external force $P = 3\,000$ lb is shown in Figure 15.

In order to verify the accuracy of the shell FE based method a very detail 3D FE stress analysis was also
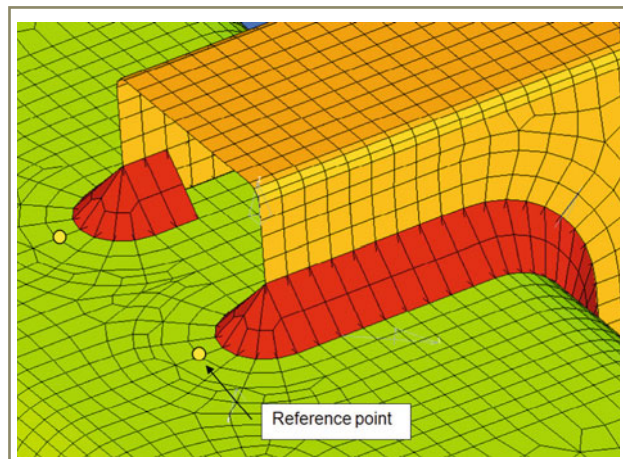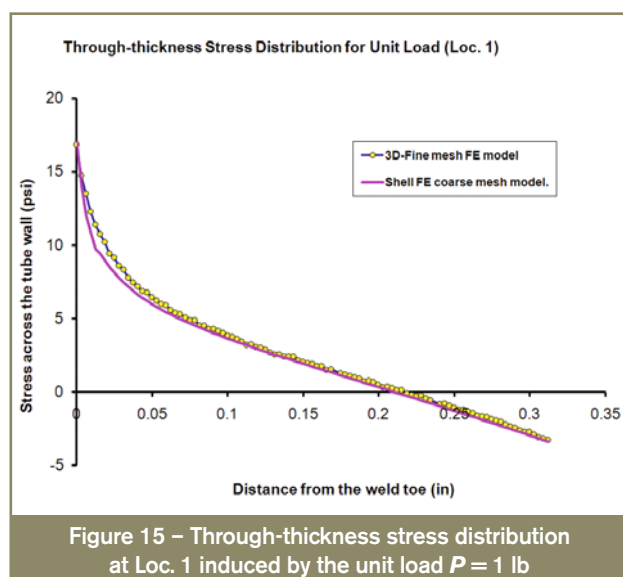

Figure 15 – Through-thickness stress distribution at Loc. 1 induced by the unit load $P = 1$ lb

carried out for the same welded joint. The through-thickness stress distribution obtained from the 3D fine mesh FE model (Figure 16) is also shown in Figure 15. It can be noted that the stress distribution obtained from the coarse mesh shell FE model and Monahan's equations coincide very well with the stress distribution obtained from the very detail and fine 3D FE mesh model of the same joint showing good accuracy of the proposed methodology. Similar results were obtained for a variety of other welded structures.

In addition to the FE calculations of the through-thickness stress distribution induced by the applied load P (Figure 12) several X-ray measurements of welding residual stresses were carried out on a few full scale welded joints. Based on the X-ray measurements and the force and bending moment equilibrium requirements the approximate through-thickness residual stress distribution at the hot spot Location 1 has been estimated and it is shown in Figure 17. The actual maximum residual stress distribution measured in the closed proximity of the reference point (Figures 11 and 13) in as-welded joints was $\sigma_{r0} = 45$ ksi.

11

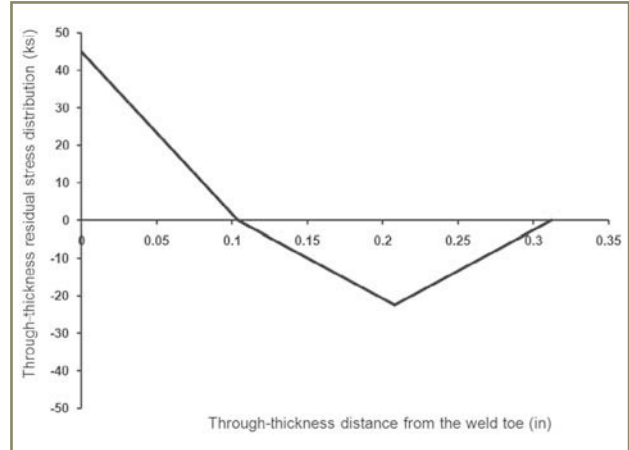Figure 16 – Details of the 3D fine mesh FE model of the critical location

Figure 17 – Through-thickness residual stress distribution at Location 1

9 Experimental and theoretical fatigue analyses

The fatigue life was predicted as a sum of the crack initiation life (the strain-life method) and crack propagation life (the fracture mechanics approach). In order to compare predicted lives with the experimental data, two series of tests were carried out. The first one was conducted at the fully reversed cyclic load of ± 3 000 lb and the other at ± 4 000 lb.

All experiments were carried out under the load control conditions and the crack length *2c*, visible on the surface, was measured versus the number of applied load cycles. Optical measurements with the aid of magnifying glass were carried out throughout all tests.

The peak stresses at the weld toe and the through-thickness stress distributions induced by the applied loads were obtained by scaling the stress distribution of Figure 12, obtained for the unit load $P = 1$ lb, by factor 3000 and 4000.

9.1 Fatigue crack initiation life analysis of tested welded joints

The fatigue crack initiation life was predicted using the in-house FALIN fatigue software with implemented strain-life fatigue live prediction procedure. The procedure is briefly described in Section 6. The elastic-plastic stresses and strains at the weld toe were calculated for each load cycle based on the Ramberg-Osgood stress strain curve (13) and the Neuber Equation (12). These strains and stresses were used in the Smith, Watson, and Topper (SWT) strain-life Equation (20) for calculating the fatigue life to crack

initiation. The fatigue crack initiation life calculations were based on the material properties listed below.

The monotonic and fatigue (cyclic) properties of the A22-H steel material are listed in Table 1 and Table 2 respectively.

The resultant amplitude of the fully reversed ($R=$ -1) cyclic stress at the weld toe Location 1 obtained from the linear elastic analysis was $\sigma_a = 51.27$ ksi and $\sigma_a = 68.36$ ksi for the load 3 000 lb and 4 000 lb respectively.

The assessed fatigue crack initiation lives, N_i, are listed in Tables 3 and 4. Unfortunately comparison of calculated fatigue crack initiation lives with experimental data is not very meaningful because the method itself does not specify what crack size corresponds to the end of rather vaguely defined crack initiation period. Therefore an engineering definition of the crack initiation size, based on experimental data, needs to be employed. The experimental data analysed by the authors up to date indicated that the predicted fatigue crack initiation lives coincided most often with lives (number of cycles) needed for the creation at the weld toe of semi-elliptical cracks of depth $a_i=0.02$ in with the aspect ratio $a_i/c_i=0.286$.

Table 2 – The cyclic and fatigue properties of the A22-H steel material

Fatigue strength coefficient (σ'_f) [ksi]	169.98
Fatigue strength exponent (*b*)	-0.12
Fatigue ductility coefficient (ε'_f)	0.648
Fatigue ductility exponent (*c*)	-0.543
Cyclic strength coefficient (*K'*) [ksi]	155.2
Cyclic strain hardening exponent (*n'*)	0.187

Table 1 – Monotonic mechanical properties of the A22-H steel material

Ultimate strength (S_u) [ksi]	Yield strength (S_y) [ksi]	Elastic modulus (*E*) [ksi]
79.0	68.89	29 938

The fatigue crack analyses were carried out for two load levels (3 000 lb and 4 000 lb) with and without residual stresses. The residual stress was combined with the cyclic stress induced by the applied load by including it [20, 21] into the Neuber or ESED equation in such a way that only the actual maximum elastic-plastic strain and stresses at the weld toe were affected.

$$\frac{\left(\sigma_{peak,max} + \sigma_{r0}\right)^2}{E} = \sigma_{max}^a \varepsilon_{max}^a - \text{the Neuber rule} \qquad (29)$$

$$\frac{\left(\sigma_{peak,max} + \sigma_{r0}\right)^2}{2E} = \frac{\left(\sigma_{max}^a\right)^2}{2E} + \frac{\sigma_{max}^a}{n'+1}\left(\frac{\sigma_{max}^a}{K'}\right)^{\frac{1}{n'}} - \text{the ESED rule} \qquad (30)$$

The magnitudes of the elastic-plastic strain and stress ranges were not affected by the static residual stress and they can be determined according to Equations (16-17) or (20-21).

It is noticeable (see Tables 3 and 4) that the residual stress had profound effect on the fatigue crack initiation life. The analysis indicates that the tensile residual stress at the weld toe may decrease the fatigue crack initiation life by approximately factor of 3.

9.2 The fatigue crack growth analysis

The second part of the fatigue life assessment was devoted to the fracture mechanics based analysis of fatigue crack growth. The fatigue crack growth analysis was carried out using the in-house FALPR software package enabling the calculation of stress intensity factors based on the weight function method and subsequent cycle by cycle fatigue crack growth increments. The observed fatigue cracks were semi-elliptical in shape (Figure A2) with initial dimensions of $a_i = 0.02$ in and $2c_i = 0.14$ in, i.e. the initial aspect ratio was $a/c = 0.238$. The semi-elliptical surface crack in a finite thickness plate was assumed to be the appropriate model for fatigue crack growth simulations.

The stress intensity factors for the actual crack shape (a/c) and depth, a, were calculated using the weight function given by Equations (A1-A50). Stress intensity factors and crack increments at points A and B (Figure A2) were simultaneously calculated on cycle by cycle basis. As a result the crack growth and the crack shape evolution were simultaneously simulated.

The through-thickness stress distribution induced by the external load shown in Figure 15 and the residual stress of Figure 17 were used for the determination of stress intensity factors. The crack increments induced by subsequent load cycles were calculated by using the Paris fatigue crack growth Equation (24) valid for $R = 0.5$ with parameters:

$m = 3.02$ and $C = 2.9736 \times 10^{-10}$ for ΔK in [ksi√in] and da/dN in [in/cycle].

The threshold stress intensity range and the fracture toughness for this material were:

$\Delta K_{th} = 3.19$ ksi√in at $R = 0$ and $K_C = 72.81$ ksi√in.

It should be noted that the crack was not growing with the same rate in all directions. Therefore crack increments at the deepest point A and those on the surface (point B Figure A2) were determined separately for each cycle. The crack dimensions and the crack aspect ratio (a/c) were updated after each load cycle. The fatigue crack growth predictions were carried out first neglecting and secondly including the residual stress effect.

In order to account for the residual stress effect the method described in reference [21] and the modified Paris equation accounting for the stress ratio R were used.

$$da / dN = C \left(U \cdot \Delta K\right)^m \qquad (31)$$

The U parameter accounting for the stress ratio effect was given by Kurihara [22] for a wide range of stress ratios in the form of Equation (32)

$$U = \frac{1}{1.5 - R} \quad \text{for} \quad -5.0 \leq R \leq 0.5$$
$$U = 1 \qquad \text{for} \quad R > 0.5 \qquad (32)$$

First the maximum and minimum stress intensity factors for a given loading cycle were determined using the weight function Equation (A9) and Equation (A33) and the load induced stress distribution $\sigma(x)$ shown in Figure 15.

$$K_{max} = \int_0^a \sigma_{max}\left(x\right) \cdot m\left(x,a\right) \cdot dx$$
$$\qquad (33)$$
$$K_{min} = \int_0^a \sigma_{min}\left(x\right) \cdot m\left(x,a\right) \cdot dx$$

Then the stress intensity factor contributed by the residual stress $\sigma_r(x)$ shown in Figure 17 was also calculated using the same weight functions given by Equation (A9) and Equation (A33).

$$K_r = \int_0^a \sigma_r\left(x\right) \cdot m\left(x,a\right) \cdot dx \qquad (34)$$

Finally all stress intensity factors were combined and the effective stress ratio was determined.

$$R_{eff} = \frac{K_{min} + K_r}{K_{max} + K_r} \qquad (35)$$

The effective stress ratio enabled to determine the actual value of the U parameter in Equation (31) and calculate the crack increment induced by analyzed loading cycle. This process was carried out analysed simultaneously for both points A and B (Figure A2) of the semi-elliptical surface crack.

An example of the crack depth growth versus the number of applied loading cycles (a vs. N), the evolution of the crack aspect ratio (a/c vs. N) and the evolution of the crack from its initial to the final shape are show in Figure 18. The experiments and fatigue crack calculations were carried out until the crack reached approximate
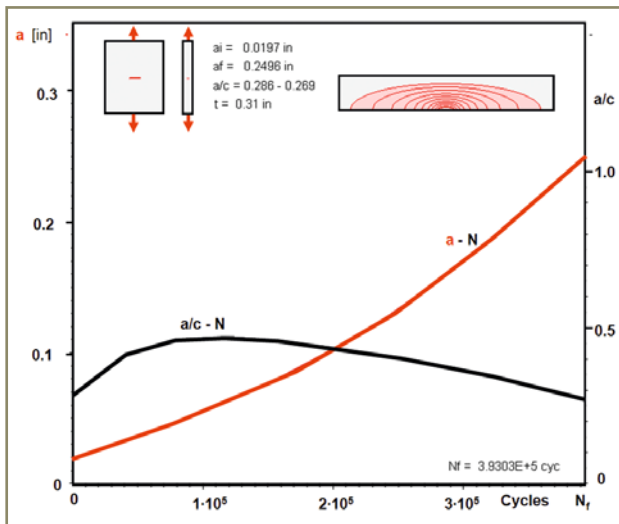
13

Figure 18 – Fatigue crack growth curve, *a* vs. *N*; evolution of the crack aspect ratio *a/c* vs. *N* and evolution of the crack shape; obtained for load 3 000 lb and $\sigma_{r0} = 0$

Figure 19 – Experimental surface crack measurements of the crack length '2c' on seven specimens and predicted '2c vs. N' curves obtained under the cyclic load of ± 4 000 lb

depth of $a_f = 0.14$ in. The numerical analyses were carried out using the following geometrical dimensions (see Figure 5) of the weld:

$t = 0.312$ in, $t_p = 3t = 0.936$ in, $h = 0.312$ in, $h_p = 0.312$ in, $r = 0.0312$ in and $\Theta = 45°$.

Statistical analysis was performed on large number (more than 100 measurements) of measured real weld toe radii and weld angles and the most frequent values given above were used for the numerical analyses. All calculated fatigue crack growth lives are summarized in Tables 3 and 4. In addition fatigue crack lengths 2c versus number of applied load cycles *N* measured on seven specimens and those calculated ones are shown in Figure 19.

Summaries of predicted fatigue crack growth periods are given in Tables 3 and 4.

The *a/c* vs. *N* curve shown in Figure 18 indicated that the crack was initially growing faster into the depth direction but after reaching the aspect ratio of approximately *a/c* = 0.5 it started growing faster along the weld toe tending to the single edge crack geometry. This conclusion is supported by the actual shape of the final crack (Figure 20) after break-opening one of the specimens.
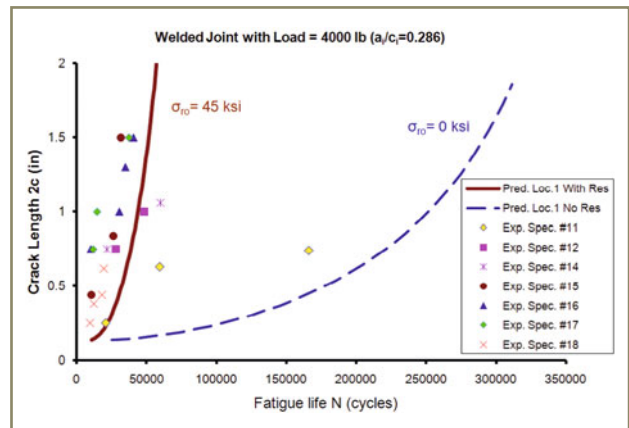
It is clear that assuming constant aspect ratio for easier fatigue crack growth analysis may contribute to significant error. Moreover, the surface crack measurements without any supporting theoretical crack growth simulations are not sufficient for reliable estimation of the crack depth 'a'.

According to the data above the ratio of the crack initiation to the crack propagation life $N_i / N_p \leq 0.303$ and the crack initiation life to the total fatigue life $N_i / N_f \leq 0.233$ were rather low (and) indicating that majority of the fatigue life of analysed weldment was spent on propagating the
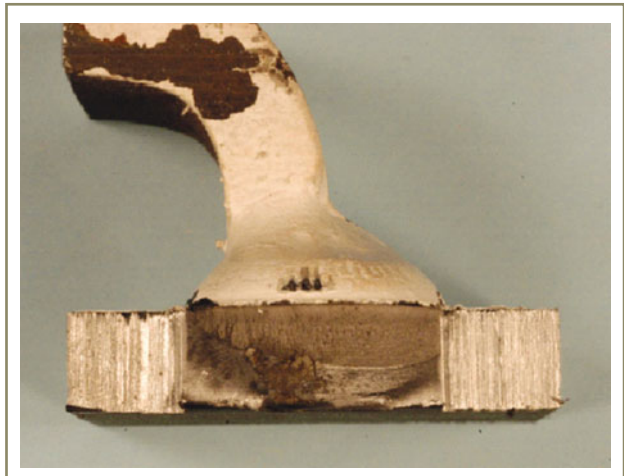

Figure 20 – The final shape of the fatigue crack initiated at the weld toe around the edge of the rectangular tube

Table 3 – Summary of predicted fatigue lives under load *P* = 3 000 lb

Residual stress [ksi]	N_i (Cycles) $a_i = 0.02$ in	N_p (Cycles) $a_f = 0.14$ in	N_i/N_p	N_f (Cycles)	N_i/N_f
$\sigma_{r0} = 0$	93 105	683 000	0.136	776 105	0.12
$\sigma_{r0} = 45$	27 939	92 000	0.303	119 939	0.233

Table 4 – Summary of predicted fatigue lives under load *P* = 4 000 lb

Residual stress [ksi]	N_i (Cycles) $a_i = 0.02$ in	N_p (Cycles) $a_f = 0.14$ in	N_i/N_p	N_f (Cycles)	N_i/N_f
$\sigma_{r0} = 0$	25 039	286 500	0.087	311 539	0.08
$\sigma_{r0} = 45$	10 602	49 975	0.212	60 577	0.175

crack from its initial crack depth $a_i = 0.02$ in to the final one $a_f = 0.14$ in.

The residual stress effect seems also to be significant. The final fatigue life was reduced by the residual stress by approximately factor of 5.

The theoretical fatigue life assessments were generally in good agreement with the experimental data for both the low and high load levels. The predicted fatigue lives were well inside the 95 % reliability scatter band.

It was also found that the predicted fatigue crack initiation lives were sensitive to the choice of the weld toe radius r. However, it has been found that the variability of the weld toe radius is not the only factor influencing the fatigue crack initiation life. It was also found that the frequency of occurrence of the smallest radius per unit length of the weld toe line, i.e. how close or how frequent along the weld toe line were located the spots with the smallest weld toe radii, had also visible effect on the final fatigue lives of tested welded joints. The distribution of spots with the smallest weld toe radius, determining the proximity of early fatigue crack initiation sites, had noticeable effect on the initial fatigue crack shape evolution and subsequent fatigue crack growth life.

10 Conclusions

An efficient shell finite element technique for obtaining stress data in welded structures relevant for fatigue analyses has been proposed. According to the proposed method the entire welded structure can be modelled using a relatively small number of large shell finite elements. The modelling technique captures both the magnitude and the gradient of the hot spot stress near the weld toe which are necessary for calculating the stress concentration and the peak stress at critical cross-sections, e.g. at the weld toe.

A procedure for the determination of the magnitude of the peak stress at the weld toe using the classical stress concentration factors (one for axial load and one for bending) has been laid proposed. The approach is based on the decomposition of the hot spot stress into the membrane and bending contribution. The method can be successfully applied to any combination of loading and weldment geometry. The stress concentration factors are used together with the hot spot membrane and bending stress σ_{hs}^m and σ_{hs}^b at the location of interest in order to determine the peak stress at the weld toe and the through-thickness non-linear stress distribution.

The knowledge of the peaks stress at the weld toe enables application of the strain-life methodology for the assessment of the fatigue crack initiation life. The through-thickness stress distribution is the base for calculating stress intensity factors with the help of appropriate weight functions. Therefore the through-thickness stress

distribution and the weight function method can be used for simulating the growth of fatigue cracks.

The validation of the proposed technique resulted in confirming good accuracy of the proposed method. In the case of the tube-on-tube welded joint subjected to torsion and bending load the shell finite element model underestimated the peak stress at the analysed location by approximately 5 % in comparison with very detail 3D fine mesh finite element analysis.

References

[1] Marshall P.W.: Design of welded tubular connections, Elsevier, Amsterdam, 1992.

[2] Dong P.: A structural stress definition and numerical implementation for fatigue analysis of welded joints, International Journal of Fatigue, 2001, vol. 23, no. 10, pp. 865-876.

[3] Niemi E.: Stress determination for fatigue analysis of welded components, Doc. IIS/IIW-1221-93, Abington Publishing, Cambridge, UK, 1995.

[4] Ryachin V.A. and Moshkariev G.N.: Durability and stability of welded structures in construction and earth moving machinery (and road building machines), Mashinostroyenie, Moskva, 1984 (in Russian).

[5] Trufyakov V.I. (editor): The strength of welded joints under cyclic loading, Naukova Dumka, Kiev, ed. V. I., 1990 (in Russian).

[6] Young J.Y. and Lawrence F.V.: Analytical and graphical aids for the fatigue design of weldments, Fracture and Fatigue of Engineering Materials and Structures, 1985, vol. 8, no. 3, pp. 223-241.

[7] Iida K. and Uemura T.: Stress concentration factor formulas widely used in Japan, IIW Doc. XIII-1530-94, 1994.

[8] Fayard J.L., Bignonnet A. and Dang Van K.: Fatigue design criteria for welded structures, Fatigue and Fractures of Engineering Materials and Structures, 1996, vol. 19, no. 6, pp. 723-729.

[9] Neuber H.: Theory of stress concentration for shear-strained prismatic bodies with arbitrary non-linear stress-strain law, ASME Journal of Applied Mechanics, ASME, 1961, vol. 28, pp. 544-551.

[10] Molski K., Glinka G.: A method of elastic-plastic stress and strain calculation at a notch root, Materials Science and Engineering, 1981, vol. 50, no. 1, pp. 93-100.

[11] Manson S.S.: Behaviour of materials under conditions of thermal stress, 1953, NACA TN-2933 and Coffin L.F. Jr., Transactions of the ASME, 1954, vol. 76, p. 931.

15

[12] Smith KN, Watson P, Topper TH.: A stress–strain function for the fatigue of metals, Journal of Materials, 1970, vol. 5, no. 4, pp. 767-778.

[13] Monahan C.C.: Early fatigue cracks growth at welds, Computational Mechanics Publications, Southampton UK, 1995.

[14] Bueckner H.F.: A novel principle for the computation of stress intensity factors, Zeitschrift fur Angewandte Mathematik Und Mechanik, 1970, vol. 50, pp. 529-546.

[15] Glinka G. and Shen G.: Universal features of weight functions for cracks in Mode I, Engineering Fracture Mechanics, 1991, vol. 40, no. 6, pp. 1135-1146.

[16] Paris P.C. and Erdogan F.: A critical analysis of crack propagation laws, Journal of Basic Engineering, 1963, no. D85, pp. 528-534.

[17] Noroozi A.H., Glinka G. and Lambert S.: A two parameter driving force for fatigue crack growth analysis, International Journal of Fatigue, 2005, vol. 27, no. 10-12, pp. 1277-1296.

[18] Mikheevskiy S. and Glinka G.: Elastic–plastic fatigue crack growth analysis under variable amplitude loading spectra, International Journal of Fatigue, 2009, vol. 31, no. 11-12, pp. 1828-1836.

[19] Murakami Y.: Stress intensity factors handbook, 1987, vol. 2, Pergamon Press, Oxford.

[20] Glinka G.: Residual stresses in fatigue and fracture: Theoretical analyses and experiments, Advances in Surface Treatments, vol. 4, A. Niku-Lari, Ed., International Journal of Residual Stresses, 1987, pp. 413-454.

[21] Glinka G.: Effect of residual stresses on fatigue crack growth in steel weldments under constant and variable amplitude loading, Fracture Mechanics, ASTM STP 677, C.W. Smith, Ed., American Society for Testing and Materials, 1979, pp. 198-214.

[22] Kurihara M., Katoh A. and Kwaahara M.: Analysis on fatigue crack growth rates under a wide range of stress ratio, Journal of Pressure Vessel Technology, Transactions of the ASME, May 1986, vol. 108, no. 2, pp. 209-213.

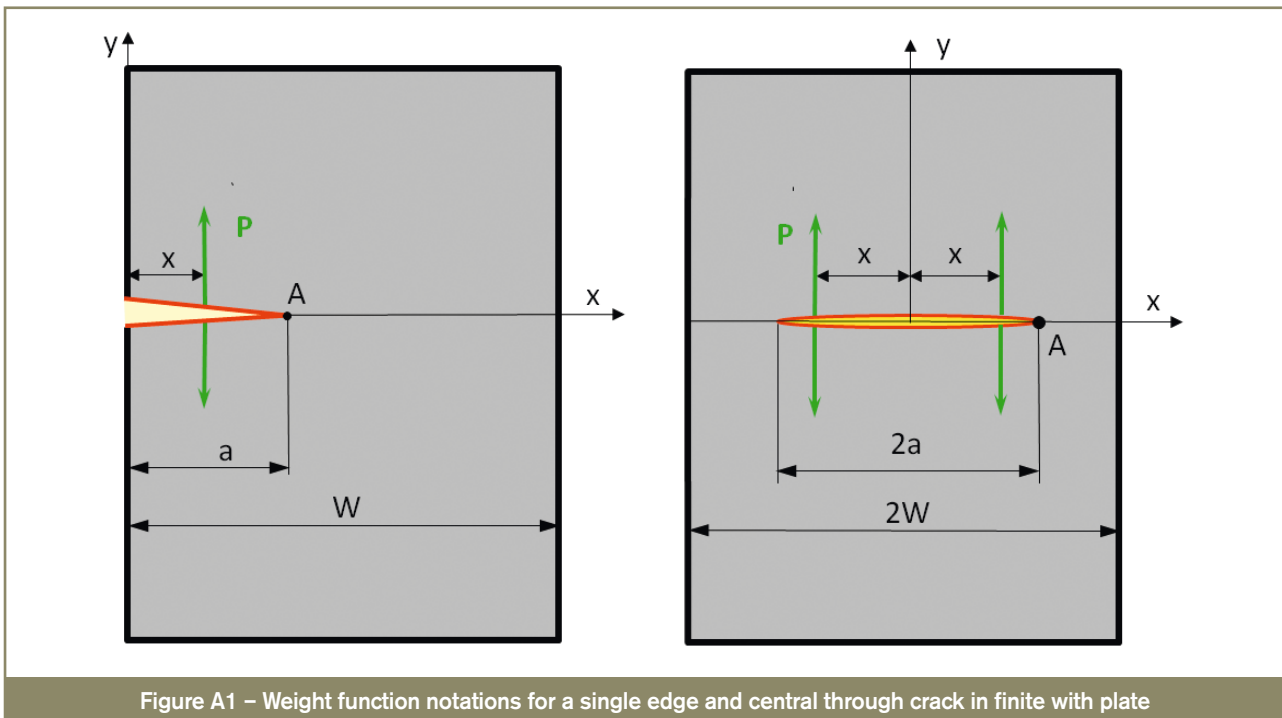## Appendix - Selected one-dimensional (1D) weight functions for cracks in plates

Figure A1 – Weight function notations for a single edge and central through crack in finite with plate

Single edge crack in a finite with plate (Figure A1, valid for $0 < a/t < 0.9$)

$$m(x,a) = K_A^F = \frac{2F}{\sqrt{2\pi(a-x)}}\left\{1 + M_1\left(1-\frac{x}{a}\right)^{\frac{1}{2}} + M_2\left(1-\frac{x}{a}\right) + M_3\left(1-\frac{x}{a}\right)^{\frac{3}{2}}\right\} \tag{A1}$$

$$M_1 = \frac{-0.029207 + \frac{a}{t}\left(0.213074 + \frac{a}{t}\left(-3.029553 + \frac{a}{t}\left(5.901933 - \frac{a}{t}2.657820\right)\right)\right)}{1.0 + \frac{a}{t}\left(-1.259723 + \frac{a}{t}\left(-0.048475 + \frac{a}{t}\left(0.481250 + \frac{a}{t}\left(-0.526796 + \frac{a}{t}0.345012\right)\right)\right)\right)} \tag{A2}$$

$$M_2 = \frac{0.451116 + \frac{a}{t}\left(3.462425 + \frac{a}{t}\left(-1.078459 + \frac{a}{t}\left(3.558573 - \frac{a}{t}7.553533\right)\right)\right)}{1.0 + \frac{a}{t}\left(-1.496612 + \frac{a}{t}\left(0.764586 + \frac{a}{t}\left(-0.659316 + \frac{a}{t}\left(0.258506 + \frac{a}{t}0.114568\right)\right)\right)\right)} \tag{A3}$$

$$M_3 = \frac{0.427195 + \frac{a}{t}\left(-3.730114 + \frac{a}{t}\left(16.276333 + \frac{a}{t}\left(-18.799956 + \frac{a}{t}14.112118\right)\right)\right)}{1.0 + \frac{a}{t}\left(-1.129189 + \frac{a}{t}\left(0.033758 + \frac{a}{t}\left(0.192114 + \frac{a}{t}\left(-0.658242 + \frac{a}{t}0.554666\right)\right)\right)\right)} \tag{A4}$$

Central through crack under symmetric stress field (Figure A1, valid for $0 < a/t < 0.9$)

$$m(x,a) = K_A^F = \frac{2F}{\sqrt{2\pi(a-x)}}\left\{1 + M_1\left(1-\frac{x}{a}\right)^{\frac{1}{2}} + M_2\left(1-\frac{x}{a}\right) + M_3\left(1-\frac{x}{a}\right)^{\frac{3}{2}}\right\} \tag{A5}$$

$$M_1 = m_1 - 200.699\left(\frac{a}{t}\right)^4 + 395.552\left(\frac{a}{t}\right)^5 - 377.939\left(\frac{a}{t}\right)^6 + 140.218\left(\frac{a}{t}\right)^7 \tag{A6}$$

$$m_1 = 0.06987 + 0.40117\left(\frac{a}{t}\right) - 5.5407\left(\frac{a}{t}\right)^2 + 50.0886\left(\frac{a}{t}\right)^3$$
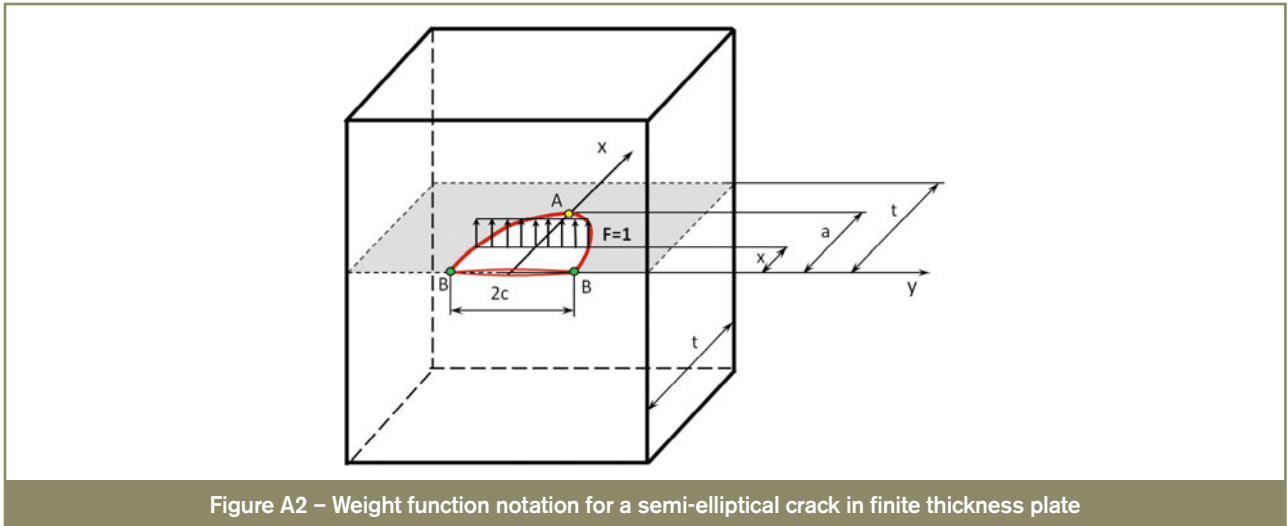
$$M_2 = m_2 + 210.599\left(\frac{a}{t}\right)^4 - 239.445\left(\frac{a}{t}\right)^5 + 111.128\left(\frac{a}{t}\right)^6 \tag{A7}$$

$$m_2 = -0.09049 - 2.14886\left(\frac{a}{t}\right) + 22.5325\left(\frac{a}{t}\right)^2 - 89.6553\left(\frac{a}{t}\right)^3$$

$$M_3 = m_3 - 347.255\left(\frac{a}{t}\right)^4 + 457.128\left(\frac{a}{t}\right)^5 - 295.882\left(\frac{a}{t}\right)^6 + 68.1575\left(\frac{a}{t}\right)^7 \tag{A8}$$

$$m_3 = 0.427216 + 2.56001\left(\frac{a}{t}\right) - 29.6349\left(\frac{a}{t}\right)^2 + 138.4\left(\frac{a}{t}\right)^3$$

Surface semi-elliptical crack (valid for 0 < a/t < 0.8, and 0 < a/c < 1, Figure A2)

Figure A2 – Weight function notation for a semi-elliptical crack in finite thickness plate

– For the deepest point A

$$m_A(x,a) = \frac{2F}{\sqrt{2\pi(a-x)}}\left\{1 + M_1\left(1-\frac{x}{a}\right)^{\frac{1}{2}} + M_2\left(1-\frac{x}{a}\right) + M_3\left(1-\frac{x}{a}\right)^{\frac{3}{2}}\right\} \tag{A9}$$

$$M_{1A} = \frac{\pi}{\sqrt{2Q}}(4Y_0 - 6Y_1) - \frac{24}{5} \tag{A10}$$

$$M_{2A} = 3 \tag{A11}$$

$$M_{3A} = 2\left(\frac{\pi}{\sqrt{2Q}}Y_0 - M_{1A} - 4\right) \tag{A12}$$

where, for 0 < a/c < 1:

$$Q = 1.0 + 1.464\left(\frac{a}{c}\right)^{1.65} \tag{A13}$$

$$Y_0 = B_0 + B_1\left(\frac{a}{t}\right)^2 + B_2\left(\frac{a}{t}\right)^4 + B_3\left(\frac{a}{t}\right)^6 \tag{A14}$$

$$B_0 = 1.0929 + 0.2581\left(\frac{a}{c}\right) - 0.7703\left(\frac{a}{c}\right)^2 + 0.4394\left(\frac{a}{c}\right)^3 \tag{A15}$$

18

$$B_1 = 0.456 - 3.045\left(\frac{a}{c}\right) + 2.007\left(\frac{a}{c}\right)^2 + \frac{1.0}{0.147 + \left(\frac{a}{c}\right)^{0.688}}$$

(A16)

$$B_2 = 0.995 - \frac{1.0}{0.027 + \left(\frac{a}{c}\right)} + 22.0\left(1 - \frac{a}{c}\right)^{9.953}$$

(A17)

$$B_3 = -1.459 + \frac{1.0}{0.014 + \frac{a}{c}} - 24.211\left(1 - \frac{a}{c}\right)^{8.071}$$

(A18)

and

$$Y_1 = A_0 + A_1\left(\frac{a}{t}\right)^2 + A_2\left(\frac{a}{t}\right)^4 + A_3\left(\frac{a}{t}\right)^6$$

(A19)

$$A_0 = 0.4537 + 0.1231\left(\frac{a}{c}\right) - 0.7412\left(\frac{a}{c}\right)^2 + 0.4600\left(\frac{a}{c}\right)^3$$

(A20)

$$A_1 = -1.652 + 1.665\left(\frac{a}{c}\right) - 0.534\left(\frac{a}{c}\right)^2 + \frac{1.0}{0.198 + \left(\frac{a}{c}\right)^{0.846}}$$

(A21)

$$A_2 = 3.418 - 3.126\left(\frac{a}{c}\right) - \frac{1.0}{0.041 + \left(\frac{a}{c}\right)} + 17.259\left(1.0 - \frac{a}{c}\right)^{9.286}$$

(A22)

$$A_3 = -4.228 + 3.643\left(\frac{a}{c}\right) + \frac{1.0}{0.020 + \frac{a}{c}} - 21.924\left(1.0 - \frac{a}{c}\right)^{9.203}$$

(A23)

19

and for $1 < a/c < 2$

$$Q = 1.0 + 1.464\left(\frac{c}{a}\right)^{1.65}\left(\frac{a}{c}\right)^2$$

(A24)

$$Y_0 = B_0 + B_1\left(\frac{a}{t}\right)^2 + B_2\left(\frac{a}{t}\right)^4$$

(A25)

$$B_0 = 1.12 - 0.09923\left(\frac{a}{c}\right) + 0.02954\left(\frac{a}{c}\right)^2$$

(A26)

$$B_1 = 1.138 - 1.134\left(\frac{a}{c}\right) + 0.3073\left(\frac{a}{c}\right)^2$$

(A27)

$$B_2 = -0.9502 + 0.8832\left(\frac{a}{c}\right) - 0.2259\left(\frac{a}{c}\right)^2$$

(A28)

$$Y_1 = A_0 + A_1\left(\frac{a}{t}\right)^2 + A_2\left(\frac{a}{t}\right)^4$$

(A29)

$$A_0 = 0.4735 - 0.2053\left(\frac{a}{c}\right) + 0.03662\left(\frac{a}{c}\right)^2$$

(A30)

$$A_1 = 0.7723 - 0.7265\left(\frac{a}{c}\right) + 0.1837\left(\frac{a}{c}\right)^2$$

(A31)

$$A_2 = -0.2006 - 0.9829\left(\frac{a}{c}\right) + 1.237\left(\frac{a}{c}\right)^2 - 0.3554\left(\frac{a}{c}\right)^3$$

(A32)

– For the surface point B

$$m_B(x,a) = \frac{2F}{\sqrt{\pi x}}\left[1 + M_{1B}\left(\frac{x}{a}\right)^{\frac{1}{2}} + M_{2B}\left(\frac{x}{a}\right)^{1} + M_{3B}\left(\frac{x}{a}\right)^{\frac{3}{2}}\right]$$

(A33)

$$M_{1B} = \frac{\pi}{\sqrt{4Q}}(30F_1 - 18F_0) - 8$$

(A34)

$$M_{2B} = \frac{\pi}{\sqrt{4Q}}(60F_0 - 90F_1) + 15$$

(A35)

$$M_{3B} = -(1 + M_{1B} + M_{2B})$$

(A36)

where for $0 < a/c < 1$:

$$F_0 = \left[C_0 + C_1\left(\frac{a}{t}\right)^2 + C_2\left(\frac{a}{t}\right)^4\right]\sqrt{\frac{a}{c}}$$

(A37)

$$C_0 = 1.2972 - 0.1548\left(\frac{a}{c}\right) - 0.0185\left(\frac{a}{c}\right)^2$$

(A38)

$$C_1 = 1.5083 - 1.3219\left(\frac{a}{c}\right) + 0.5128\left(\frac{a}{c}\right)^2$$

(A39)

$$C_2 = -1.101 + \frac{0.879}{0.157 + \frac{a}{c}}$$

(A40)

and

$$F_1 = \left[D_0 + D_1\left(\frac{a}{t}\right)^2 + D_2\left(\frac{a}{t}\right)^4\right]\sqrt{\frac{a}{c}}$$

(A41)

$$D_0 = 1.2687 - 1.0642\left(\frac{a}{c}\right) + 1.4646\left(\frac{a}{c}\right)^2 - 0.7250\left(\frac{a}{c}\right)^3$$

(A42)

$$D_1 = 1.1207 - 1.2289\left(\frac{a}{c}\right) + 0.5876\left(\frac{a}{c}\right)^2$$

(A43)

$$D_2 = 0.190 - 0.608\left(\frac{a}{c}\right) + \frac{0.199}{0.035 + \frac{a}{c}}$$

(A44)

and for $1 < a/c < 2$

$$F_0 = \left[C_0 + C_1\left(\frac{a}{t}\right)^2 + C_2\left(\frac{a}{t}\right)^4\right]\sqrt{\frac{a}{c}}$$

(A45)

$$C_0 = 1.34 - 0.2872\left(\frac{a}{c}\right) + 0.0661\left(\frac{a}{c}\right)^2$$

(A46)

$$C_1 = 1.882 - 1.7569\left(\frac{a}{c}\right) + 0.4423\left(\frac{a}{c}\right)^2$$

(A47)

$$C_2 = -0.1493 + 0.01208\left(\frac{a}{c}\right) + 0.02215\left(\frac{a}{c}\right)^2$$

(A48)

and

$$F_1 = \left[D_0 + D_1\left(\frac{a}{t}\right)^2 + D_2\left(\frac{a}{t}\right)^4\right]\sqrt{\frac{a}{c}}$$

(A49)

$$D_0 = 1.12 - 0.2442\left(\frac{a}{c}\right) + 0.06708\left(\frac{a}{c}\right)^2 \qquad\qquad (A50)$$

$$D_1 = 1.251 - 1.173\left(\frac{a}{c}\right) + 0.2973\left(\frac{a}{c}\right)^2 \qquad\qquad (A51)$$

$$D_2 = 0.04706 - 0.1214\left(\frac{a}{c}\right) + 0.04406\left(\frac{a}{c}\right)^2 \qquad\qquad (A52)$$

About the authors

Mr. Aditya CHATTOPADHYAY (achattop@uwaterloo.ca) is with University of Waterloo, Faculty of Engineering, Waterloo, Ontario (Canada). Dr. Grzegorz GLINKA (gggreg@mecheng1.uwaterloo.ca) is also with University of Waterloo, Faculty of Engineering, Waterloo, Ontario (Canada) as well as with Aalto University, Helsinki (Finland). Dr. Mohamad EL-ZEIN (el-zeinmohamads@johndeere.com), Dr. Jin QIAN (QianJin@JohnDeere.com) and Mr. Rodrigo FORMAS (FormasRodrigoG@JohnDeere.com) are all with Deere & Company World Headquarters, Moline, Illinois (United States).

21